INFALL REGIONS OF GALAXY CLUSTERS

Antonaldo Diaferio[1] and Margaret J. Geller

Harvard-Smithsonian Center for Astrophysics, 60 Garden Street Cambridge, MA 02138

ABSTRACT

In hierarchical clustering, galaxy clusters accrete mass through the aggregation of smaller systems. Thus, the velocity field of the infall regions of clusters contains significant random motion superimposed on radial infall. Because the purely spherical infall model does not predict the amplitude of the velocity field correctly, methods estimating the cosmological density parameter Ω_0 based on this model yield unreliable biased results. In fact, the amplitude of the velocity field depends on local dynamics and only very weakly on the global properties of the universe.

We use N-body simulations of flat and open universes to show that the amplitude of the velocity field of the infall regions of dark matter halos is a direct measure of the escape velocity within these regions. We can use this amplitude to estimate the mass of dark matter halos within a few megaparsecs from the halo center. In this region dynamical equilibrium assumptions *do not* hold. The method yields a mass estimate with better than 30% accuracy. If galaxies trace the velocity field of the infall regions of clusters reliably, this method provides a straightforward way to estimate the amount of mass surrounding rich galaxy clusters from redshift data alone.

Subject headings: dark matter — galaxies: clusters: general — gravitation — methods: numerical

1.   INTRODUCTION

The linear theory of density perturbations shows that a spherically symmetric mass concentration in an expanding universe induces a radial peculiar velocity field in the surrounding region

$$\frac{v_{\rm pec}(r)}{H_0 r} = -\frac{1}{3}\Omega_0^{0.6}\delta(r) \tag{1}$$

where $\delta(r)$ is the average spherical mass overdensity within the radius r, and H_0 and Ω_0 are the Hubble constant[2] and the cosmological density parameter at the present time, respectively. We

---

[1]Present address: Max-Planck-Institut für Astrophysik, Karl-Schwarzschild-Str. 1, 85740, Garching bei München, Germany

[2]We use $h = 0.5$ throughout, where $H_0 = 100h$ km s^{-1} Mpc^{-1}.

can estimate the galaxy number overdensity $\delta_g = b\delta$ where b is the bias parameter. Thus, if we can measure $v_{\rm pec}$ we can estimate $\beta = \Omega_0^{0.6}/b$. Several authors have applied this method to the Local Supercluster and to the Virgo cluster with mixed results (see e.g. the review by Davis & Peebles 1983; see also Strauss & Willick 1995). Along with the uncertainties in the determination of the galaxy number overdensity and the peculiar velocity themselves, external tidal shear can strongly affect the velocity field (e.g. Hoffman 1986; Eisenstein & Loeb 1995; Bond & Myers 1996); thus we cannot obtain reliable results unless we sample the velocity field within the full three-dimensional region around the cluster (Villumsen & Davis 1986).

In redshift space, spherical infall confines galaxies around clusters within caustics, surfaces with a characteristic "trumpet" shape (Kaiser 1987). For these non-linear regions, we must replace the linear regime equation (1) with the exact solution of the equation of motion of shells in an overdense region within the expanding universe (e.g. Silk 1977). However, the dependence of the peculiar velocity on β and δ_g is still approximately separable (Regös & Geller 1989). Thus, provided we can determine the location of the caustics, we can still estimate β through the measurement of δ_g for a rich galaxy cluster (Regös & Geller 1989). Recently, Regös (1996) suggested the application of gravitational lensing (e.g. Tyson, Valdes, & Wenk 1990; Kaiser & Squires 1993; Kaiser, Squires, & Broadhurst 1995; Bonnet & Mellier 1995) to determine the mass overdensity δ and therefore the unbiased value of Ω_0.

Standard inflationary cosmologies (e.g. Peacock 1996) predict that the primordial density field is a Gaussian random field. These initial conditions can lead to either top-down or bottom-up scenarios for the formation of cosmic structures. The hierarchical clustering in the bottom-up scenarios, with large systems forming by aggregation of smaller ones, currently represents the most successful framework of structure formation theories as it seems to be able to reproduce many, although not all, properties of the real universe. The top-down scenarios are far less succesfull (see e.g. Padmanabhan 1993 for a general discussion).

The general formation process of clusters in hierarchical scenarios differs substantially from the one described by the idealized spherical model; here clusters form through the infall of smooth spherical shells onto an initial density peak (Gunn & Gott 1972). Despite its idealized nature, the spherical model appears to represent a reasonable description of the collapse of high peaks in a random Gaussian density field (Bernardeau 1994), and predicts density and velocity profiles of final systems in reasonably good agreement with N-body simulations of dark matter halo formation when the power spectrum has an effective spectral index $n \geq -1$ (Zaroubi, Naim, & Hoffman 1996). These authors suggest that particle ranks in binding energy are conserved during the formation process. This conservation is responsible for the agreement (see also Hoffman 1988; Quinn & Zurek 1988; Zaroubi & Hoffman 1993). In fact, for spectral indices $n \leq -1$ the formation process is more violent (Lynden-Bell 1967), energy ranks are not conserved, and the agreement breaks down.

Thus, the agreement in energy space between the spherical infall model and hierarchical clustering for a limited range of spectral index, n, allows correct predictions about the *final state* of

the halo. However, the spherical infall model does not describe the *evolution* of the outer regions of systems in configuration space. N-body simulations of flat universes (van Haarlem 1992; van Haarlem & van de Weygaert 1993) show that the velocity field of cluster surroundings is very different from the predictions of spherical infall because (1) recent mergers increase the particle kinetic energy, and (2) the presence of substructures makes the velocity profile irregular. In other words, random motions obscure the infall information. If the same problem arises in real galaxy clusters, estimates of β (or Ω_0) based on spherical infall are systematic overestimates.

Here, we suggest a unifying explanation for the amplitude of the caustics. We use N-body simulations of flat and open universes to show that the escape velocity around dark matter halos determines the amplitude of the caustics. Thus, the local dynamics of the halo, not the global properties of the universe, dominates the amplitude of the velocity field around clusters.

We also show that under reasonable hypotheses about the density field outside the virialized region, the velocity field around a cluster provides an estimate of the mass enclosed within a few megaparsecs of the cluster center. This method is particularly interesting because, in this region, the equilibrium assumptions underlying usual mass estimation methods do not hold.

In Sect. 2 we review the main equations of the spherical infall model. In Sect. 3 we derive the alternative expression for the amplitude of the caustics and we outline the mass estimation method. In Sect. 4 we compare both the expression for the amplitude of the caustics and the spherical infall model with the results of N-body simulations. We also use these N-body simulations to test our new mass estimation method.

2.   THE SPHERICAL INFALL MODEL

We now review the main points of the infall model for a spherical perturbation in the case of open and flat universes. We then define the infall region and the caustic surfaces surrounding the perturbation.

Consider a spherical perturbation in an expanding universe described by the average overdensity profile $\delta_i(< r_i)$ within the physical radius r_i at time $a_i \ll 1$, where a is the cosmological scale factor, $a = 1$ at the present time, and $\delta_i \ll 1$ for any radius r_i. The evolution of each shell in the absence of shell crossings is described by the equation of motion $d^2r/dt^2 = -GM/r^2 + \Lambda r/3$, where M is the mass within r, Λ is the cosmological constant, and G is the gravitational constant. The first integral of the equation of motion is

$$\frac{1}{2}\left(\frac{dr}{dt}\right)^2 - \frac{GM}{r} - \frac{\Lambda}{6}r^2 = E \tag{2}$$

where E is the total energy of the shell. In order to consider the collapse independent of the primordial density profile, we can think in terms of the local scale factor $x = ra_i/r_i$. Note that at time a_i, $x = a_i$ for all the shells. However, at later times, if we assume that δ_i is a monotonically

decreasing function of r_i, the degeneracy between x and r_i disappears, and we have a biunique correspondence between x and δ_i. With this change of variable, equation (2) becomes

$$\dot{x}^2 - \frac{\alpha}{x} - \Omega_{\Lambda 0} x^2 = e \tag{3}$$

where the dot indicates a derivative with respect to $\tau = H_0 t$, $\Omega_{\Lambda 0} = \Lambda/3H_0^2$, and

$$\alpha(\delta_i) \;=\; \Omega_0(1 + \delta_i) \tag{4}$$

$$e(\delta_i) \;=\; 1 - \Omega_{\Lambda 0} - \Omega_0 \left(1 + \frac{5}{3}\frac{\delta_i}{a_i}\right). \tag{5}$$

In deriving equation (5) for the effective energy $e = (2E/H_0^2)(a_i/r_i)^2$, we set the initial conditions at time $a_i \sim 10^{-3}$, when linear theory in a matter-dominated universe is a good description of the growth of perturbations. In other words, we assume that at this epoch the decaying modes of the perturbation have decayed away and the peculiar velocity field v_i has reached the amplitude predicted by linear theory, $v_i/H_i r_i = -\Omega_{0i}^{0.6}\delta_i/3$, where H_i is the Hubble constant and Ω_{0i} is the cosmological density parameter at time a_i (see e.g. Lilje & Lahav 1991). Thus, to first order in δ_i, the peculiar velocity field contributes the term $-2\Omega_0\Omega_{0i}^{0.6}\delta_i/3a_i$ to the effective total energy. In equation (5) we have further assumed $\Omega_{0i} = \Omega_0/[\Omega_0 + (1 - \Omega_0 - \Omega_{\Lambda 0})a_i + \Omega_{\Lambda 0}a_i^3] \simeq 1$, when $a_i \sim 10^{-3} \ll 1$.

When $\Omega_{\Lambda 0} < 0$, the shell always collapses. Otherwise, for collapse to occur, the effective energy e must satisfy

$$e < \begin{cases} -3\Omega_{\Lambda 0}(\alpha/2\Omega_{\Lambda 0})^{2/3} & \Omega_{\Lambda 0} > 0 \\ 0 & \Omega_{\Lambda 0} = 0. \end{cases} \tag{6}$$

The smallest positive root (or the only positive root when $\Omega_{\Lambda 0} < 0$) of the cubic equation $\Omega_{\Lambda 0}x^3 + ex + \alpha = 0$ gives the maximum expansion scale factor $x_{\max}(\delta_i)$ of the shell with internal overdensity δ_i. Thus, we may write the collapse time

$$\tau_{\text{coll}}(\delta_i) = 2 \int_0^{x_{\max}(\delta_i)} \frac{dy}{\dot{x}(y, \delta_i)}. \tag{7}$$

Finally, we can write the equation describing the evolution of $x(\delta_i, \tau)$ implicitly

$$\tau = \begin{cases} \int_0^{x(\delta_i,\tau)} dy/\dot{x}(y, \delta_i) & 0 \leq \tau \leq \tau_{\text{coll}}/2 \\ \tau_{\text{coll}}(\delta_i) - \int_0^{x(\delta_i,\tau)} dy/\dot{x}(y, \delta_i) & \tau_{\text{coll}}/2 < \tau \leq \tau_{\text{coll}}. \end{cases} \tag{8}$$

In terms of the local scale factor x, we next determine the caustics which depend only on the cosmological parameters and not on the overdensity profile. Consider the spherical perturbation within space $X = (x, \theta, \varphi)$, where θ and φ are the azimuthal and longitudinal angle, respectively. In the following, we use the terms "distance" and "velocity" to indicate the quantities x and $\dot{x}$, respectively. Recall that $x = ra_i/r_i$. Thus, we need the initial average overdensity profile $\delta_i(< r_i)$ to transform space X into configuration space $R = (r, \theta, \varphi)$, and to obtain the physical distance r and the physical velocity $v = dr/dt$.

Now, suppose we project the spherical perturbation within space X onto the plane $\theta = \pi/2$. We can measure the projected distance $x_\perp$ from the origin, the longitudinal angle φ and the velocity component $\dot{x}_3$ along the axis $\theta = 0$. The relations between the new and the old variables are

$$x_\perp = x(\delta_i, \tau)\sin\theta, \quad \dot{x}_3 = \dot{x}(x, \delta_i)\cos\theta, \quad \varphi = \varphi. \tag{9}$$

Suppose we observe the spherical perturbation at a time, τ. From the equations $\tau_{\rm coll}(\delta_i^c) = \tau$ and $\tau_{\rm coll}(\delta_i^m) = 2\tau$ (eq. [7]) we can determine the primordial overdensity δ_i^c of the shell which has just collapsed and the δ_i^m of the shell which is at maximum expansion at time τ. Thus, the local scale factor of the perturbation at turnaround is $x_{\rm ta} = x_{\rm max}(\delta_i^m)$. To determine the virial scale factor at time τ we need to consider the virial theorem (see e.g. Lahav et al. 1991). We have $e = -\alpha/2x_v - 2\Omega_{\Lambda 0}x_v^2$ in virial equilibrium, and $e = -\alpha/x_m - \Omega_{\Lambda 0}x_m^2$ for the *same* shell at maximum expansion. Energy conservation implies

$$2\eta\psi^3 - (2+\eta)\psi + 1 = 0 \tag{10}$$

where $\psi = x_v/x_m$ and $\eta = 2\Omega_{\Lambda 0}x_m^3/\alpha$. Note that we can also write $\eta = \Lambda/4\pi G\rho_m$, where ρ_m is the mean density of the perturbation within $r_m = r_i x_m/a_i$. The condition for collapse is $\eta < 1$, and we are interested in the solution $\psi \leq 1$ of equation (10) with η a free parameter. We have

$$\psi(\eta) = \begin{cases} 2p^{1/3}\cos[\arccos(q/p)/3] & \eta \leq \eta_0 \\ (q + \Delta^{1/2})^{1/3} + (q - \Delta^{1/2})^{1/3} & \eta_0 < \eta < 0 \\ 1/2 & \eta = 0 \\ 2p^{1/3}\cos[\arccos(q/p)/3 + 4\pi/3] & 0 < \eta < 1 \end{cases} \tag{11}$$

where $p = [(2+\eta)/6\eta]^{3/2}$, $q = -1/4\eta$, $\Delta = q^2 - p^2$, and $\eta_0 \simeq -6.427$ is the only real solution of the cubic equation $\Delta = 0$.

Now we can write the virial scale factor $x_{\rm vir}$ at time τ, $x_{\rm vir} = \psi(\eta)x_{\rm max}(\delta_i^c)$ where $\eta = 2\Omega_{\Lambda 0}x_{\rm max}^3(\delta_i^c)/\Omega_0(1 + \delta_i^c)$. We define the infall region of the perturbation at time τ as the region within the scale factor range $(x_{\rm vir}, x_{\rm ta})$. Note that $x_{\rm vir}$ and $x_{\rm ta}$ are the virial scale factor and the turnaround scale factor of two *different* shells of the perturbation.

At fixed $x_\perp \in (x_{\rm vir}, x_{\rm ta})$, the velocity component $\dot{x}_3$ depends only on θ, $\dot{x}_3 = \dot{x}[x_\perp/\sin\theta, \delta_i(\theta)]\cos\theta$ (see eqs. [9] and [3]), where $\delta_i(\theta)$ satisfies the implicit equation (see eq. [8])

$$\tau = \tau_{\rm coll}[\delta_i(\theta)] - \int_0^{x_\perp/\sin\theta} \frac{dy}{\dot{x}[y, \delta_i(\theta)]}. \tag{12}$$

Thus, the extrema of $\dot{x}_3$ occur at $\theta = \theta_{\rm max}(x_\perp, \tau)$, and $\theta = \pi - \theta_{\rm max}(x_\perp, \tau)$ which satisfy the equation $d\dot{x}_3/d\theta = 0$. Note that $\theta_{\rm max}$ is almost independent of the cosmology.

In the plane $(x_\perp, \dot{x}_3)$ the perturbation fills only the region within the curves

$$\dot{x}_3^2(x_\perp, \tau) = \dot{x}^2\{x[\delta_i(\theta_{\rm max}), \tau]\}\cos^2\theta_{\rm max} \tag{13}$$

which determine the caustics. For any $x_\perp$, the maximum difference in the velocity component $\dot{x}_3$ is the difference between the velocities on the caustics, $\Delta \dot{x}_3(x_\perp, \tau) = 2|\dot{x}_3(x_\perp, \tau)|$.

To switch from space X to configuration space R, we must take the initial average overdensity profile $\delta_i(< r_i)$ into account. However, at any time, the physical radius is $r = x r_i / a_i$ and the radial velocity is $v/H_0 r = \dot{x}/x$. The peculiar velocity is $v_{\rm pec}/H_0 r = v/H_0 r - H/H_0$, where H is the Hubble constant at time τ. Thus, for the velocity difference on the caustics, we have $\Delta \dot{x}_3/x_\perp = \Delta v_3/H_0 r_\perp$, where $r_\perp$ is the projected physical radius along the line of sight. Therefore, if we define the amplitude of the velocity field $\mathcal{A}_v = \Delta v_3/2$, we can see that the observable quantity $\mathcal{A}_v/H_0 r_\perp$ coincides with the quantity $\Delta \dot{x}_3/2 x_\perp$ we have in space X. Fig. 1 shows the profile of the amplitude of the velocity field vs. the local scale factor $x_\perp$ of the projected physical radius $r_\perp$ for different values of $[\Omega_0, \Omega_{\Lambda 0}]$ at the present time. We have $r_\perp/r_{\rm vir} = (x_\perp/x_{\rm vir})(r_\perp/r_{\rm vir})_{a=a_i}$ and a monotonically decreasing $\delta_i(< r_i)$; thus we must stretch these curves out according to $\delta_i(< r_i)$ in order to obtain the observable profiles. Note that $x_{\rm ta}/x_{\rm vir} \lesssim 2^{5/3}$ is almost constant for $\Omega_{\Lambda 0} = 0$ universes. In particular, we have $r_{\rm ta}/r_{\rm vir} = (x_{\rm ta}/x_{\rm vir})(r_{\rm ta}/r_{\rm vir})_{a=a_i} \gtrsim 3$ in the absence of shell crossings.

Fig. 1 shows that the caustic amplitude depends on $[\Omega_0, \Omega_{\Lambda 0}]$, as expected. However, for fixed $x_\perp$ the dependence is weak: $\partial \ln \dot{x}/\partial \ln \Omega_0 \sim 0.3$. We recover the usual 0.6 logarithmic dependence, when we switch to physical distances $r_\perp$.

3. ESCAPE VELOCITY AND MASS ESTIMATE

In redshift space, the infall regions of halos in N-body experiments resemble the characteristic trumpet shapes expected in the spherical infall model (e.g. van Haarlem & van de Weygaert 1993; Jing & Börner 1996). However, the amplitude of these caustics, namely the difference between the maximum and minimum line-of-sight velocity at projected distance $r_\perp$ from the halo center, usually exceeds the amplitude predicted by the model. The larger amplitude occurs because of random motions in the infall region.

In §3.1, we derive an expression for the amplitude of the velocity field which takes random motions into account. This expression indeed replaces the prediction of the spherical infall model. Moreover, this expression suggests a method of estimating the mass enclosed within a distance $r_\perp$ from the halo center, where $r_\perp$ extends well beyond the region of virial equilibrium. We derive this expression in §3.2. In §4, we compare both expressions with N-body simulations of dark matter halos.

3.1. Amplitude of the velocity field

Consider a dark halo in its center of mass reference frame. Consider the velocity anisotropy parameter at position $\mathbf{r}$ from the halo center

$$\beta(\mathbf{r}) = 1 - \frac{\langle v_t^2 \rangle}{2\langle v_r^2 \rangle} \tag{14}$$

where v_r is the radial component of the particle velocity $\mathbf{v}$, $v^2 = v_t^2 + v_r^2$, and $\langle \cdot \rangle$ indicates an average over the velocities of all particles within the volume $d^3\mathbf{r}$ centered on position $\mathbf{r}$. Within the virialized region $r < r_\delta$, where r_δ is some virial radius (see §4.2.1), particle motion is mainly random and $\beta \sim 0$. For $r > r_\delta$, orbits become more radial and β increases up to ~ 0.8 (see §4.2.1). Within these regions, random motions still contribute significantly to the velocity field, because of the intrinsic stochastic accretion process in hierarchical clustering. The non-zero $\langle v_t^2 \rangle$ at large radii is responsible for the general increase of the amplitude of the caustics relative to pure spherical infall.

In order to write down an expression for the amplitude of the velocity field, we note that the presence of random motions in the outskirts of the halo implies that encounters can give a particle enough energy to escape the gravitational field of the halo. Thus, if the random motion is significant, we expect that the amplitude of the velocity field at a given distance r *is* the line-of-sight component of the escape velocity, not the smaller velocity induced solely by spherically symmetric infall.

The escape velocity is $v_{\mathrm{esc}}^2(\mathbf{r}) = -2\phi(\mathbf{r})$: the caustic amplitude is thus a measure of the gravitational potential $\phi(\mathbf{r})$. For the sake of simplicity, consider a spherical system. We have

$$v_{\mathrm{esc}}^2(r) = -2\phi(r) = \frac{2GM(<r)}{r} + 8\pi G \int_r^\infty \rho(x)x\,dx \tag{15}$$

where $M(<r)$ is the total mass within r and $\rho(r)$ is the system density profile. Equation (15) holds regardless of the stability of the system.

In equation (15) v_{esc} is the full three-dimensional escape velocity. Observations of real clusters will provide only the component $v_{\mathrm{l.o.s.}}$ of the escape velocity along the line-of-sight at projected distances $r_\perp$. The velocity field within the infall region is not isotropic, as indicated by the large value of the anisotropy parameter, $\beta \gtrsim 0.5$. If the tangential component $v_t(r_\perp)$ of the velocity field is isotropic, we have $\langle v_t^2 \rangle = 2\langle v_{\mathrm{l.o.s.}}^2 \rangle$,[3] or

$$\langle v_{\mathrm{esc}}^2(r_\perp) \rangle = \langle v_{\mathrm{l.o.s.}}^2(r_\perp) \rangle \frac{3 - 2\beta(r_\perp)}{1 - \beta(r_\perp)}. \tag{16}$$

In §4.2.2, we will see that equation (16) indeed describes the amplitude of the velocity field of dark matter halos out to a few times the virial radius, r_δ.

---

[3] We are assuming that $v_{\mathrm{esc}}^2(r)$ is a non-increasing function of r. This behavior is valid for density profiles steeper than r^{-1}.

3.2. Mass estimate

We now argue that the measure of the escape velocity along the line of sight, i.e. the measure of the amplitude of the caustics, may provide a method to estimate $M(< r)$. In principle, knowledge of v_{esc} readily yields an estimate of the mass within r from equation (15),

$$2GM(< r) = -r^2 \frac{dv_{\mathrm{esc}}^2}{dr}. \tag{17}$$

However, v_{esc}^2 is the product of two functions (eq. [16]). The anisotropy parameter $\beta(r_\perp)$ is unknown, but suppose we can model it. The only measurable function $v_{\mathrm{l.o.s.}}^2(r_\perp)$ is likely to be very noisy. Thus, differentiation of v_{esc}^2 is not practical.

We thus consider an alternative approach. Consider a shell with mass $dm = 4\pi\rho r^2 dr$. Assuming $\langle v_{\mathrm{esc}}^2 \rangle = -2\phi(r)$, we may write

$$dm = -2\pi \langle v_{\mathrm{esc}}^2 \rangle \frac{\rho(r)r^2}{\phi(r)} dr. \tag{18}$$

The mass surrounding the halo is

$$GM(< r) - GM(< r_\delta) = \int_{r_\delta}^{r} \langle v_{\mathrm{esc}}^2(x) \rangle \widetilde{\mathcal{F}}(x) dx \tag{19}$$

where we introduce the filling function $\widetilde{\mathcal{F}}(r) = -2\pi G\rho(r)r^2/\phi(r)$. Here, we integrate the noisy function rather than differentiating it.

We now replace, in equation (19), the three-dimensional distance r with the projected distance $r_\perp$, and the three-dimensional escape velocity v_{esc} with the measurable $v_{\mathrm{l.o.s.}}$. The second replacement implies the introduction of the velocity field anisotropy parameter β. Equation (19) becomes

$$GM(< r_\perp) - GM(< r_\delta) = \int_{r_\delta}^{r_\perp} \langle v_{\mathrm{l.o.s.}}^2(x) \rangle \mathcal{F}(x) dx \tag{20}$$

where

$$\mathcal{F}(x) = \widetilde{\mathcal{F}}(x) \frac{3 - 2\beta(x)}{1 - \beta(x)}. \tag{21}$$

Knowledge of the filling function $\mathcal{F}$ allows the estimation of the system mass for any $r_\perp \in (0, \infty)$. However, we need to know $\mathcal{F}$ precisely only for $r_\perp < r_\delta$. For $r_\perp > r_\delta$ we may consider $\mathcal{F}$ as a free function, generally slowly varying when $r_\perp/r_\delta \in (1, 3)$, where we expect to apply equation (20). In fact, the assumption of a spherically symmetric $\rho(r)$ leading to equation (20) is a very crude approximation at best. Thus, the complete expression in equation (21) for $\mathcal{F}$ might not be a robust representation of the filling function. On the other hand, we will see in §4.2.3 that equation (20) still holds for reasonable models of $\mathcal{F}$. In practice, we can estimate the mass within r_δ by applying the virial theorem or by assuming hydrostatic equilibrium of the X-ray emitting gas. Outside r_δ these methods break down, and we can use equation (20).

Reasonable assumptions about the behavior of ρ and ϕ at large radii provide a model for $\widetilde{\mathcal{F}}$. For example, if we neglected the integral in equation (15), we would have $\rho \propto r^{-3}$, $\phi \propto r^{-1}$, and $\widetilde{\mathcal{F}} = \text{const}$. A universal density profile suggested by Navarro, Frenk & White (1995) for dark matter halos is

$$\rho(r) = \frac{\rho_0 r_s^3}{r(r + r_s)^2} \tag{22}$$

where r_s is some scale length. This profile yields

$$\widetilde{\mathcal{F}}(r) = \frac{r^2}{(r + r_s)^2} \frac{1}{2 \ln(1 + r/r_s)}. \tag{23}$$

This profile is a good fit for $r \lesssim r_\delta$ only. Gravitational lensing observations show that this model reproduces real cluster profiles within 1 Mpc[4] (Tormen, Bouchet, & White 1996). However, the model may be a poor approximation in the cluster outskirts.

To obtain $\mathcal{F}$, we can assume $\beta(r) \sim \text{const} \sim 0.6 - 0.8$. Despite this crude approximation to $\mathcal{F}$, we now show that, for suitable choices of $\mathcal{F}$, the method outlined here can lead to remarkably good mass estimates for N-body systems.

4. N-BODY SIMULATIONS

We now use N-body simulations to illustrate how random motions in the outskirts of dark halos invalidate application of the spherical infall model to estimate Ω_0. We also show that measurement of the amplitude of the velocity field *does* provide a method of obtaining the enclosed mass with better than 30% accuracy for massive halos.

4.1.   Simulation Parameters

As typical hierarchical clustering scenarios, we consider three Cold Dark Matter (CDM) universes with $[\Omega_0, \Omega_{\Lambda 0}] = [1.0, 0.0], [0.2, 0.0], [0.2, 0.8]$, and $h = 0.5$. Initial conditions are generated with the COSMOS package developed by E. Bertschinger (1995) which perturbs initial particle positions and velocities from a grid according to the Zel'dovich approximation. We produce a realization of the Gaussian random field of the initial density perturbations with the Bardeen et al. (1986) power spectrum containing the transfer function for adiabatic fluctuations and negligible baryon density. We normalize the power spectrum with $\sigma_8 = 1.0$ at the present time, where σ_8 is the rms matter density fluctuation in spheres of radius 16 Mpc. This value of σ_8 is between the values required to fit the observed abundance of local clusters in critical and flat low-density CDM universes (White, Efstathiou, & Frenk 1993). We simulate a 50^3 Mpc^3 periodic volume with 64^3 particles.

---

[4]All distances in this paper are for $h = 0.5$.

The number density of Abell clusters with richness $R \geq 1$ is $\sim 10^{-6}$ Mpc^{-3} (e.g. Scaramella et al. 1991); thus we need constrained initial conditions to obtain a rich cluster within the simulation box. We generate constrained random fields with the algorithm of Hoffman & Ribak (1991) in the implementation of van de Weygaert & Bertschinger (1996). We are interested only in the presence of a rich cluster at the center of the box. Thus, we specify only the height δ_p of the local density maximum. Specifically, we choose $\delta_p = 3\sigma(R_G)$, where $\sigma^2(R_G)$ is the variance of the density field smoothed with a Gaussian filter of radius $R_G = 4$ Mpc.

We integrate the equations of motion with a particle-mesh code (Hockney & Eastwood 1981, Efstathiou et al. 1985) using 128^3 mesh points, a seven-point finite-difference approximation to the Laplacian, a cloud-in-cell density assignment, a leap-frog integrator, and an energy conserving scheme to compute the force. CDM universes have an effective spectral index $n \sim -1$ on cluster scales. Thus, we use the scale factor a as the time variable (Efstathiou et al. 1985). We also use this variable for the open models, though this choice is actually appropriate only for flat universes. Simulations obtained with different integration variables a^α with $\alpha \in [0.5, 1.5]$ do not yield appreciably different results. Simulations run from $a \sim 0.02$ to the present time $a = 1$ with ~ 700 timesteps. The mesh and the poor momentum conservation of our code produce force anisotropies which prevent the Layzer-Irvine cosmic energy equation from being satisfied to better than $\sim 10\%$ over the entire simulation, even for timesteps smaller than the timestep we used. However, the computed force follows the Newtonian value accurately for distances roughly twice the mesh cell size, ~ 0.4 Mpc in our simulations.

Our simulations have two main shortcomings: (1) poor spatial resolution and integration accuracy, and (2) small box size. Despite the first problem, we will see in the next subsection that for distances larger than the cell size, our halos roughly reproduce the density and velocity fields obtained in simulations with larger dynamical range and higher accuracy (Tormen et al. 1996). At any rate, we are currently running another set of simulations with the AP^{3}M code (Couchman 1991) made available by Hugh Couchman and collaborators (Couchman, Thomas, & Pearce 1995) and we will report on these results in a forthcoming paper. The second problem, namely the small box size, implies less tractable errors.

First, periodic boundary conditions produce artificial tidal forces from replicas of structures within the simulation box. The constrained random field clearly aggravates this problem. Artificial tidal forces erroneously increase the random motions in the outskirts of halos; they thus artificially worsen the prediction of the spherical infall model. Gelb & Bertschinger (1994b) suggest that box sizes $L > 50$ Mpc are necessary to provide reliable results on clustering. However, in $L \sim 50$ Mpc box simulations, individual halo dynamics is almost unaffected because the artificial tidal forces are sufficiently suppressed (Gelb & Bertschinger 1994a). Thus, we expect tidal fields to be a minor problem in our models.

Secondly, we omit contributions from Fourier components of the primordial density perturbation field with wavelengths larger than the box size. Thus, we underestimate both the amplitude

of clustering and the amplitude of the peculiar velocities. Corrections to the evolved state of the simulation (Tormen & Bertschinger 1996) or correction during its evolution (Cole 1996) alleviate the problem. The missing clustering would probably increase the merger rate and therefore the random motion in the outskirts of halos, thus worsening the predictive power of the spherical infall model. The velocity field is affected mainly in the bulk velocity. Random motions increase by only a few percent when one increases the size of the box from 100 to 800 Mpc (Tormen & Bertschinger 1996).

In summary, we increase the random motions because of poor spatial resolution and integration accuracy, but we decrease it because of missing large-scale power. We plan further work to investigate how these problems affect our results.

4.2. Results

We now describe the results of our simulations. First, we consider the density and velocity fields of the most massive halos (§4.2.1). In §4.2.2, we examine the velocity field within the infall regions. We compare the simulations with the mass estimation method in §4.2.3.

4.2.1. Halo Identification

We identify halos using a generalization of the friends-of-friends algorithm (Barnes & Efstathiou 1987) with a linking length equal to 0.1 Mpc ~ 0.13 times the interparticle distance, and a critical number of neighbor particles $N_c = 10$ ($N_c = 1$ yields the classical friends-of-friends algorithm). These parameters assure a halo overdensity $\delta \sim 10^2 - 10^3$ with respect to the background. However, this point is of secondary importance; we are interested only in the determination of the center of mass of the halo in order to study the velocity field of the outer regions. Linking lengths between 0.08 and 0.16 Mpc move the center of mass of the most massive halos less than 1%. The center of mass velocity suffers larger oscillations. However, to suppress this problem we redefine the cluster velocity from all the particles within the virial radius r_δ defined below.

In the outskirts of halos, halo asphericities have little effect on particle velocities, because equipotential surfaces are rounder than equidensity surfaces. For example, van Haarlem et al. (1993) find that at distances larger than a few megaparsecs from the halo center, the force difference between a spherical distribution and a significantly ellipsoidal distribution is $\lesssim 15\%$. These authors also show that asphericities can blur the caustics expected in the infall model. However, the disagreement between the spherical infall model and the simulations is more severe than the departures induced by asphericity (see van Haarlem & van de Weygaert 1993).

We intend to compare the amplitude of the velocity field with the gravitational potential. Thus, we can assume spherically symmetry, even though halos are not spherically symmetric. Around the

halo center of mass we define spherical shells at equally spaced logarithmic intervals of distance r from the center. Spherical shells containing the same number of particles yield the same results.

In order to compare our simulations with the spherical infall model, we need to determine the region where the model is valid. Consider the halo density at virialization $\rho_h = \rho_m/\psi^3(\eta)$, where ρ_m is the halo density at maximum expansion, $\psi(\eta)$ is given by equation (11), and $\eta = 2\Omega_{\Lambda 0}x_{\max}^3(\delta_i^c)/\Omega_0(1+\delta_i^c) = \Lambda/4\pi G\rho_m$. We obtain

$$\frac{\rho_h}{\rho(a)} = \frac{2\Omega_{\Lambda 0}}{\Omega_0}\frac{a^3}{\eta\psi^3(\eta)} \tag{24}$$

where $\rho(a)$ is the mean density of the universe at time a. Note that in $\Omega_{\Lambda 0} = 0$ universes $2\Omega_{\Lambda 0}/\eta = \pi^2/\tau_{\text{coll}}^2$, and equation (24) reduces to

$$\frac{\rho_h}{\rho(a)} = \frac{8\pi^2}{\Omega_0}\frac{a^3}{\tau_{\text{coll}}^2}. \tag{25}$$

In particular, for the Einstein-de Sitter universe the overdensity of the virialized halo scales as $(1+z_f)^3$, where z_f is the formation redshift of the halo (White 1996). With equation (24) we can define the radius of the halo r_δ when the average overdensity $\delta(r)$ within the radius r satisfies $1+\delta = \rho_h/\rho(a)$. Thus, we expect the spherical infall model to be valid when $r > r_\delta$.

We now consider the halo density and velocity fields. We consider the most massive halos in the simulations at the present time $a = 1$, when they are far enough in time from major mergers which formed the final halos. Strongly unrelaxed states affect the density and velocity fields of the halos (Tormen et al. 1996) but have little effect on the predictive power of the escape velocity as we show in the next subsection.

Here we examine the halo formation in the three investigated cosmological scenarios on the basis of simulations starting with the same seed for the random number generator. Thus, we obtain roughly the same evolutionary history for the three halos. We ran another set of simulations with different seeds for the random numbers. These simulations provide similar results. Note that we use a fixed number of particles within the simulation box; thus, the halo in the flat universe with a final mass $\sim 7 \cdot 10^{14} M_\odot$ is approximately five times more massive than the most massive halos in the open universes.

At $a = 1$, the largest halos contain $\gtrsim 20,000$ particles within $r_\delta \sim 2$ Mpc, typically. The first row of Fig. 2 shows the circular velocity profile $v_{\text{circ}}(r) = [GM(<r)/r]^{1/2}$. We compare the simulated profiles with the profile

$$v_{\text{circ}}^2 = 4\pi G\rho_0 r_s^3 \left[\frac{1}{r}\ln\left(1+\frac{r}{r_s}\right) - \frac{1}{r+r_s}\right] \tag{26}$$

derived from the Navarro et al. (1995) density profile (eq. [22]). Fig. 2 shows the best fits. The agreement is acceptable, even though we fit the profile up to $r = 5r_\delta$ instead of $r \sim r_\delta$ for which equation (26) is expected to hold (Navarro et al. 1995). If we fit only the range $[0.1, 1]r_\delta$ the agreement improves slightly, though our poor resolution at small radii is more apparent.

The second row of Fig. 2 shows the anisotropy parameter $\beta(r) = 1 - \langle v_t^2 \rangle / 2 \langle v_r^2 \rangle$ (eq. [14]). When $r \gtrsim r_\delta$, β increases from ~ 0.5 to $\sim 0.6 - 0.8$, indicating predominantly radial motion. At $r \sim 5 r_\delta$, β drops to $\sim 0.2 - 0.3$ because of the presence of another halo. Note that in the flat universe, random motions dominate the velocity field more strongly than in the open universes at large r. This effect is *not* the result of the different cosmology, but of the different local dynamics and of the larger mass of the halo, which implies a larger accretion rate (see e.g. Lacey & Cole 1994; Manrique & Salvador-Solé 1996). For comparison, Fig. 2 shows $\beta(r)$ for a $\sim 2 \cdot 10^{14} M_\odot$ halo within the flat universe simulation box (dashed line). The frequency of radial orbits is larger than for the more massive halo.

Our results agree acceptably with those obtained by Tormen et al. (1996) with higher resolution simulations of a $P(k) \propto k^{-1}$ flat universe. Note that we reach only a resolution of $\sim 0.1 r_\delta$, compared with the $\sim 0.01 r_\delta$ resolution of Tormen et al. (1996).

4.2.2. *Velocity Field within the Infall Regions*

We now consider the prediction of the spherical infall model. We project the halo along a random direction and consider the amplitude of the velocity field $2 \mathcal{A}_v(r_\perp) = v_{\max} - v_{\min}$ where $v_{\max}$ and $v_{\min}$ are the maximum and minimum line-of-sight velocity at projected distance $r_\perp$ from the center of the halo. Fig. 3 shows $\mathcal{A}_v / H_0 r_\perp$ in our simulations. This quantity should agree with the spherical infall prediction for $r_\perp > r_\delta$ (dashed line). We compute this prediction using complete three-dimensional information to evaluate the overdensity and then to derive the expected velocity field. The model systematically underestimates the amplitude of the velocity field. Clearly, estimates of Ω_0 based on spherical infall *always* overestimate the actual value.

In contrast, agreement with the escape velocity $v_{\mathrm{esc}}^2 = -2 \phi(r_\perp)$ (solid line) is excellent. We compute the escape velocity through the discrete version of equation (15). We replace the upper limit of integration with a maximum radius $r_{\max}$, usually in the range $5 - 10 r_\delta$. Our results are insensitive to this parameter; $r_{\max} < 5 r_\delta$ usually underestimates the true potential. When $r_{\max} > 10 r_\delta$ the spherical assumption breaks down severely because of the presence of other halos. We finally correct for the velocity field anisotropy (eq. [16]):

$$\mathcal{A}_v^2(r_\perp) = -2 \phi(r_\perp) \frac{1 - \beta(r_\perp)}{3 - 2\beta(r_\perp)}. \tag{27}$$

The agreement is remarkable. It indicates that the gravitational potential, i.e. the local dynamics, determines the amplitude of the velocity field in the outskirts of halos. The spherical infall model is a poor predictor of the velocity field. The global density of the universe apparently plays no role.

Fig. 3 also shows that the agreement holds regardless of the dynamical state of the halos. For comparison, we show the halos at the present time (lower row), when they are approximately in equilibrium, and the halos right after the merging of the two halos of comparable size which formed

the final halos (upper row). The escape velocity, namely the gravitational potential, still follows the velocity field correctly.

4.2.3.   Estimate of the Halo Surrounding Mass

We now apply the method outlined in §3 to estimate the mass surrounding the virialized region. We suppose that we know the virial radius r_δ, the particle velocities along the line of sight, and the mass within r_δ, $M(< r_\delta)$. For real systems, we can estimate $M(< r_\delta)$ with X-ray methods or with the virial theorem. In future work we plan to investigate how the uncertainty in the virial mass affects the estimate of the mass within the infall regions.

We use equation (20), assuming two different filling functions $\mathcal{F}$, namely $\mathcal{F}_1 = 1/2$, and $\mathcal{F}_2 = [\ln(1 + \alpha r_\perp/r_\delta)]^{-1}$. $\mathcal{F}_1$ assumes that the entire gravitational potential originates within $r_\perp$. $\mathcal{F}_2$ is equation (23) with a free parameter $\alpha = r_\delta/r_s \sim 3 - 10$, typically. For $\mathcal{F}_2$, we have assumed $r^2/(r+r_s)^2 \approx 2(1-\beta)/(3-2\beta)$. This assumption is reasonable when $1 \lesssim r/r_\delta \lesssim 5$ and $\beta \sim 0.6-0.7$. Results obtained with $\alpha \in (3, 10)$ do not differ appreciably.

Fig. 4 shows the ratio between the estimated mass within the radius r, $M_{\rm est}(< r)$ and the actual mass $M(< r)$. Equation (20) is apparently a good mass estimator, at least up to $r \sim 5r_\delta$, where we start observing the velocity field of another halo. For $r < 5r_\delta$, the difference between the estimated and the actual mass is always $< 16\%$, and is $\sim 10\%$, on average. Fig. 4 shows both the "unrelaxed" (upper row) and "relaxed" state (lower row; see Fig. 3). For the relaxed state the mass estimate improves. However, the difference from the unrelaxed state is not large.

If we do not know $M(< r_\delta)$ the agreement between the estimated mass and the true mass worsens, particularly for unrelaxed states. Fig. 5 shows the halo mass estimated with equation (20) when we integrate from $r_\perp = 0$. It is remarkable that $\mathcal{F}_1$ still works reasonably well for $r_\perp < r_\delta$ when the clusters are relaxed (lower row), showing that the filling function $\mathcal{F}_1$ is more robust than $\mathcal{F}_2$. We expect this result; when $r_\perp < r_\delta$ our hypotheses leading to $\mathcal{F}_2$ break down. When the clusters are unrelaxed (upper row) the estimation method introduces large errors. These results imply only that both filling functions are inadequate; the velocity field is still well described by the escape velocity (Fig. 3).

Fig. 6 shows how our mass estimator behaves statistically. For each model, we separate the most massive from the least massive halos, regardless of their dynamical state. For the flat universe, we consider halos with $M(< r_\delta) \geq 10^{14} M_\odot$ and $10^{13} M_\odot \leq M(< r_\delta) < 10^{14} M_\odot$. For the open universes, we consider halos with $M(< r_\delta) \geq 2 \cdot 10^{13} M_\odot$ and $10^{12} M_\odot \leq M(< r_\delta) < 2 \cdot 10^{13} M_\odot$. We thus have roughly the same number of particles within each halo for the low or high mass range in both the flat and open universes. Fig. 6 shows the median of the halo mass profiles; error bars indicate the upper and lower quartile of all the profiles at each position $r_\perp/r_\delta$.

The method yields better estimates for more massive halos (upper row). The agreement for

less massive halos worsens because tidal fields caused by neighboring larger halos severely perturb the velocity fields of the smaller halos. However, these small halos contain only a few thousand particles within $r_\delta \sim$ a few times the cell size. Thus, numerical artifacts may also play a significant role.

Fig. 6 shows that our method of estimating the mass of *non-virialized* regions yields better than 30% statistical accuracy for halos with virial mass $M(< r_\delta) \gtrsim 0.5 - 1.0 \cdot 10^{14} M_\odot$. For comparison, consider the accuracy of X-ray estimates of the mass of *virialized* halos. N-body/hydrodynamics simulations show that the assumption of an isothermal gas in hydrostatic equilibrium yields virial masses with better than 20% accuracy (Navarro et al. 1995; Schindler 1996; Evrard, Metzler, & Navarro 1996). We note however that gravitational lensing methods, which do not require equilibrium assumptions, may disagree with X-ray observations. For example, Wu & Fang (1996) claim that X-ray observations may actually underestimate the mass of real clusters by a factor of $\sim$ 2. However, gravitational lensing methods suffer systematic errors due to non-spherical symmetry, projection effects, and substructure (Miralda-Escudé & Babul 1995; Bartelmann 1995). On the other hand, there are examples where X-ray mass estimates do agree with weak lensing estimates to within the error limits (see e.g. Squires et al. 1996a; Squires et al. 1996b). We conclude that when applied to N-body systems our mass estimation method has an accuracy comparable with other widely used methods.

Application of our method to real clusters introduces non-trivial challanges. First, we do not know how reliably galaxies trace the velocity field in these non-linear regions. Secondly, sampling effects may introduce large errors, though these effects can be quantified. Even if we could overcome these problems, it is not clear how reliably we can determine the amplitude of the velocity fields in cluster infall regions; the caustics may not be very apparent (e.g. van Haarlem et al. 1993). We plan to investigate these issues in future work.

5. CONCLUSION

In redshift space, galaxies around clusters should appear within regions with a characteristic trumpet shape (Kaiser 1987). Regös & Geller (1989) suggested applying the spherical infall model to these caustics to constrain the density of the universe. We show that this method generally overestimates the actual density parameter Ω_0 because random motions increase the amplitude of the caustics (see also Lilje & Lahav 1991; White & Zaritsky 1992).

We define the amplitude of the velocity field as half of the difference between the maximum and minimum line-of-sight velocity at projected distance $r_\perp$ from the cluster center. We use N-body simulations to show that the escape velocity (eqs. [15], and [27]) describes this amplitude well, with $r_\perp$ ranging over two orders of magnitude, from the central region of the halo to its infall regions, where particle orbits are mainly radial. Van Haarlem (1992) first noted that the spherical infall method overestimates Ω_0 and pointed out that mergers and substructures within the infall regions

are responsible for the disagreement. Here we suggest a unifying explanation.

We show that our interpretation of the amplitude of the velocity field within halo infall regions can be applied to estimate the interior mass of halos up to a few virial radii r_δ from the halo center, where the usual equilibrium assumptions do not hold. This estimation technique works because the local dynamics depends more strongly on the mass of the halo than on the global properties of the universe. This deduction agrees with the recent suggestion by White (1996) and Navarro, Frenk, & White (1996) that halos have a universal density profile, basically independent of the cosmology, with a characteristic density depending on the formation time of the halo (see also our eq. [25]) which ultimately depends on the halo mass. In the literature, the dependence of the density profile on the halo mass has been neglected, with attention focused on the dependence on Ω_0 and on the power spectrum $P(k)$. The limited overdensity range examined in these numerical studies explains why N-body simulations appear to show a dependence of the halo density profile on the underlying cosmology (e.g. Crone, Evrard, & Richstone 1994).

If we know the mass $M(< r_\delta)$ within the virial radius r_δ our mass estimation method can estimate the mass up to several r_δ with a $\lesssim 30\%$ uncertainty on average, at least for halos with mass $M(< r_\delta) \gtrsim 0.5 - 1.0 \cdot 10^{14} M_\odot$. If cluster galaxies are unbiased tracers of the gravitational potential, we can estimate the mass within the outskirts of observed systems on the basis of redshift data alone. However, we must investigate how sampling affects the result, and we must explore how accurately we need to know the mass within the virial radius. Last but not least, we must find a reliable method of determining the caustics and extracting the escape velocity function $v_{\rm esc}(r_\perp)$. This problem is not trivial because the caustics may not be obvious (e.g. van Haarlem et al. 1993), although they do appear in some cases (see e.g. A3266 in Quintana, Ramírez, & Way 1996, and the Coma cluster in the 15R Survey of Geller et al. 1997). On the theoretical side, we need a reasonable assumption for the filling function $\mathcal{F}$ that we can calibrate with N-body simulations. It is reassuring that the simplest assumption we investigate here, $\mathcal{F} = $ const, works reasonably well.

We plan to pursue this approach by acquiring dense redshift samples in the infall regions of nearby rich galaxy clusters in order to estimate masses on scales $\lesssim 10$ Mpc, where linear theory breaks down and where galaxy systems are not yet in virial equilibrium.

REFERENCES

Bardeen, J. M., Bond, J. R., Kaiser, N., & Szalay, A. S. 1986, ApJ, 304, 15

Barnes, J. E., & Efstathiou, G. 1987, ApJ, 319, 575

Bartelmann, M. 1995, A&A, 299, 11

Bernardeau, F. 1994, ApJ, 427, 51

Bertschinger, E. 1995, astro-ph/9506070

Bond, J. R., & Myers, S. T. 1996, ApJS, 103, 41

Bonnet, H., & Mellier, Y. 1995, A&A, 303, 331

Cole, S. 1996, MNRAS, in press (astro-ph/9604046)

Couchman, H. M. P. 1991, ApJ, 368, L23

Couchman, H. M. P., Thomas, P. A., & Pearce, F. R. 1995, ApJ, 452, 797

Crone, M. M., Evrard, A. E., & Richstone, D. O. 1994, ApJ, 434, 402

Davis, M., & Peebles, P. J. E. 1983, ARA&A, 21, 109

Efstathiou, G., Davis, M., Frenk, C. S., & White, S. D. M. 1985, ApJS, 57, 241

Eisenstein, D. J., & Loeb, A. 1995, ApJ, 439, 520

Evrard, A. E., Metzler, C. A., & Navarro, J. F. 1996, ApJ, 469, 494

Gelb, J., & Bertschinger, E. 1994a, ApJ, 436, 467

Gelb, J., & Bertschinger, E. 1994b, ApJ, 436, 491

Geller, M. J., et al. 1997, in preparation

Gunn, J. E., & Gott, J. R. 1972, ApJ, 176, 1

Hockney, R. W., & Eastwood, J. W. 1981, Computer Simulation Using Particles (New York: Mc-Graw Hill)

Hoffman, Y. 1986, ApJ, 308, 493

Hoffman, Y. 1988, ApJ, 328, 489

Hoffman, Y., & Ribak, E. 1991, ApJ, 380, L5

Jing, Y. P., & Börner, G. 1996, MNRAS, 278, 321

Kaiser, N. 1987, MNRAS, 227, 1

Kaiser, N., & Squires, G. 1993, ApJ, 404, 441

Kaiser, N., Squires, G., & Broadhurst, T. 1995, ApJ, 449, 460

Lacey, C. & Cole, S. 1994, MNRAS, 271, 676

Lahav, O., Lilje, P. B., Primack, J. R., & Rees, M. J. 1991, MNRAS, 251, 128

Lilje, P. B., & Lahav, O. 1991, ApJ, 374, 29

Lynden-Bell, D. 1967, MNRAS, 136, 101

Manrique, A., & Salvador-Solé, E. 1996, ApJ, 467, 504

Miralda-Escudé, J., & Babul, A. 1995, ApJ, 449, 18

Navarro, J. F., Frenk, C. S., & White, S. D. M. 1995, MNRAS, 275, 720

Navarro, J. F., Frenk, C. S., & White, S. D. M. 1996, ApJ, submitted (astro-ph/9611107)

Padmanabhan, T. 1993, Structure Formation in the Universe (Cambridge: Cambridge University Press)

Peacock, J. A. 1996, in The Structure of the Universe, EADN School, Leiden, in press (astro-ph/9601135)

Quinn, P. J., & Zurek, W. H. 1988, ApJ, 331, 1

Quintana, H., Ramírez, A., & Way, M. J. 1996, AJ, 112, 36

Regös, E. 1996, A&A, 308, 368

Regös, E., & Geller, M. J. 1989, AJ, 98, 755

Scaramella, R., Zamorani, G., Vettolani, G., & Chincarini, G. 1991, AJ, 101, 342

Schindler, S. 1996, A&A, 305, 756

Silk, J. 1977, A&A, 59, 53

Squires, G., Kaiser, N., Babul, A., Fahlman, G., Woods, D., Neumann, D. M., & Böringer, H. 1996a, ApJ, 461, 572

Squires, G., Neumann, D. M., Kaiser, N., Arnaud, M., Babul, A., Böringer, H., Fahlman, G., & Woods, D. 1996b, ApJ, submitted (astro-ph/9603050)

Strauss, M. A., & Willick, J. A. 1995, Phys. Rep., 1995, 261, 271

Tormen, G., & Bertschinger, E. 1996, ApJ, in press (astro-ph/9512131)

Tormen, G., Bouchet, F. R., & White, S. D. M. 1996, MNRAS, in press (astro-ph/9603132)

Tyson, J. A., Valdes, F., & Wenk, R. A. 1990, ApJ, 349, L1

van de Weygaert, R., & Bertschinger, E. 1996, MNRAS, 281, 84

van Haarlem, M. P. 1992, Ph. D. Thesis, Leiden University

van Haarlem, M. P., Cayón, L., Gutiérrez de la Cruz, C., Martinéz-González, E., & Rebolo, R. 1993, MNRAS, 264, 71

van Haarlem, M. P., & van de Weygaert, R. 1993, ApJ, 418, 544

Villumsen, J. V., & Davis, M. 1986, ApJ, 308, 499

White, S. D. M. 1996, in Gravitational Dynamics, 36th Herstmonceux Conference, ed. O. Lahav, E. Terlevich, & R. Terlevich, in press (astro-ph/9602021)

White, S. D. M., Efstathiou, G., & Frenk, C. S. 1993, MNRAS, 262, 1023

White, S. D. M., & Zaritsky, D. 1992, ApJ, 394, 1

Wu, X.-P., & Fang, L.-Z. 1996, ApJ, 467, L45

Zaroubi, S., & Hoffman, Y. 1993, ApJ, 416, 410

Zaroubi, S., Naim, A., & Hoffman, Y. 1996, ApJ, 457, 50
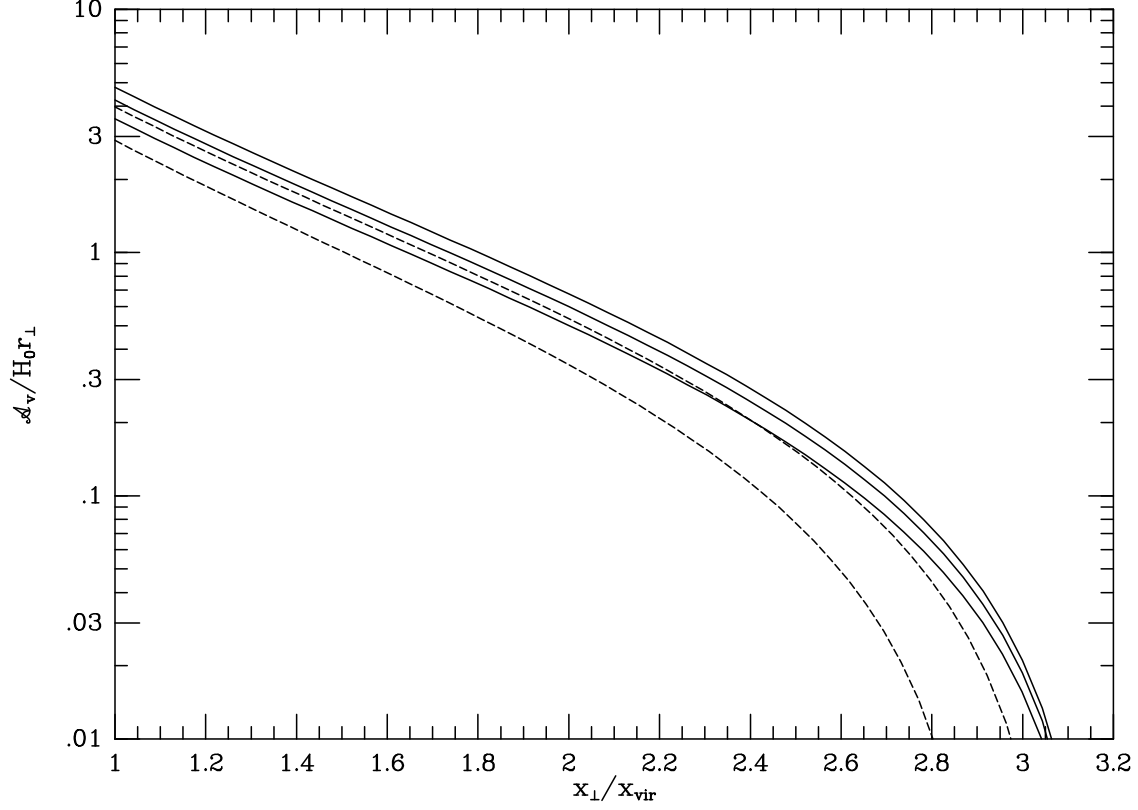
Fig. 1.— Amplitude $\mathcal{A}_v$ of the velocity field within the infall region of a spherical perturbation in an otherwise uniform universe at the present time. The amplitude is in units of the projected physical distance $r_\perp$ from the center of the perturbation; $x_\perp$ is the component perpendicular to the line of sight of the local scale factor x. From top to bottom, solid lines are for $[\Omega_0, \Omega_{\Lambda 0}] = [1.0, 0.0], [0.5, 0.0], [0.1, 0.0]$. Upper dashed line is for $[\Omega_0, \Omega_{\Lambda 0}] = [0.5, 0.5]$; lower dashed line is for $[\Omega_0, \Omega_{\Lambda 0}] = [0.1, 0.9]$.
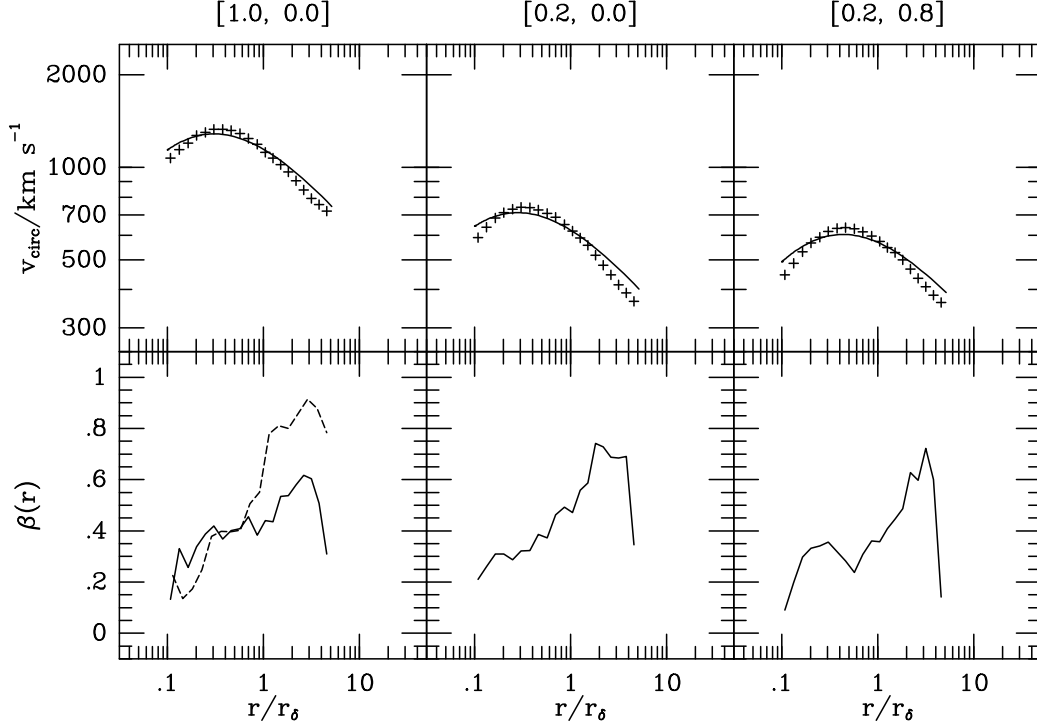
Fig. 2.— Density and velocity fields of the most massive halo in each N-body model. Upper row shows the circular velocity $v_{\rm circ} = [GM(< r)/r]^{1/2}$. Solid lines are the best fits to equation (26). Lower row shows the velocity field anisotropy parameter $\beta(r)$ (eq. [14]). The values of $[\Omega_0, \Omega_{\Lambda 0}]$ are shown over each column. The dashed line in the $[\Omega_0, \Omega_{\Lambda 0}] = [1.0, 0.0]$ model is for a halo of mass $M \sim 2 \cdot 10^{14} M_\odot$, roughly the most massive halo in the open models.
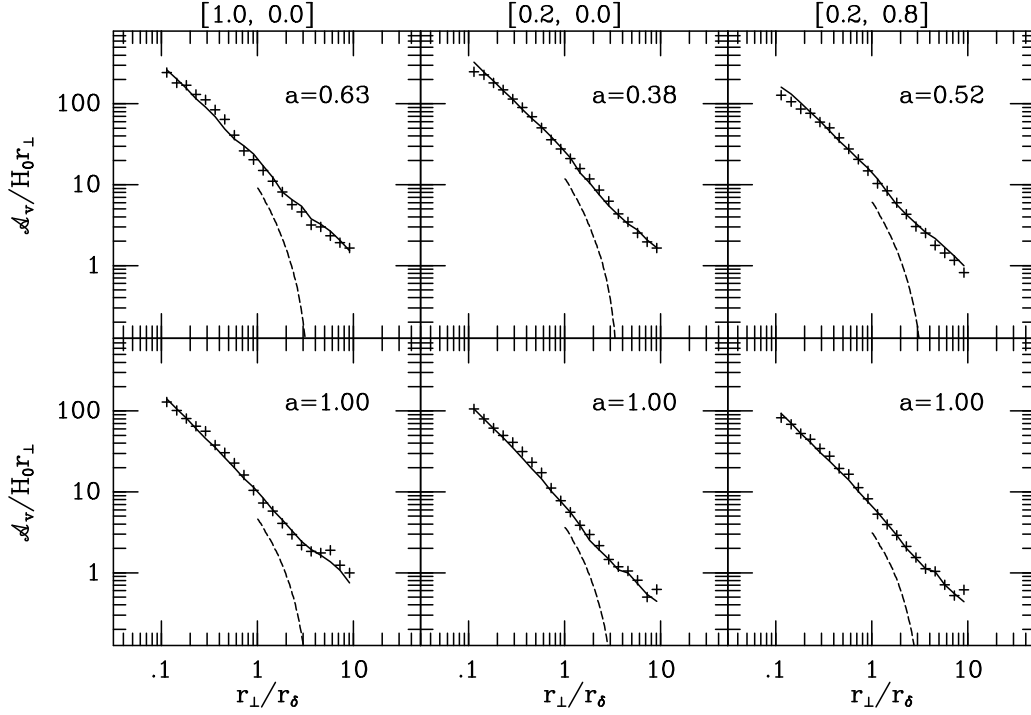
Fig. 3.— Amplitude of the velocity field within the infall region of the most massive halo in each N-body model. Solid lines are the escape velocities computed with equation (15) corrected for the anisotropy parameter with equation (16). Dashed lines are the spherical infall predictions which hold only for $r_\perp > r_\delta$. Lower row shows the halos at the present time $a = 1$, when the halos are roughly in equilibrium. Upper row shows the halos at earlier times, right after the major mergers of the two smaller halos which formed the final halos.
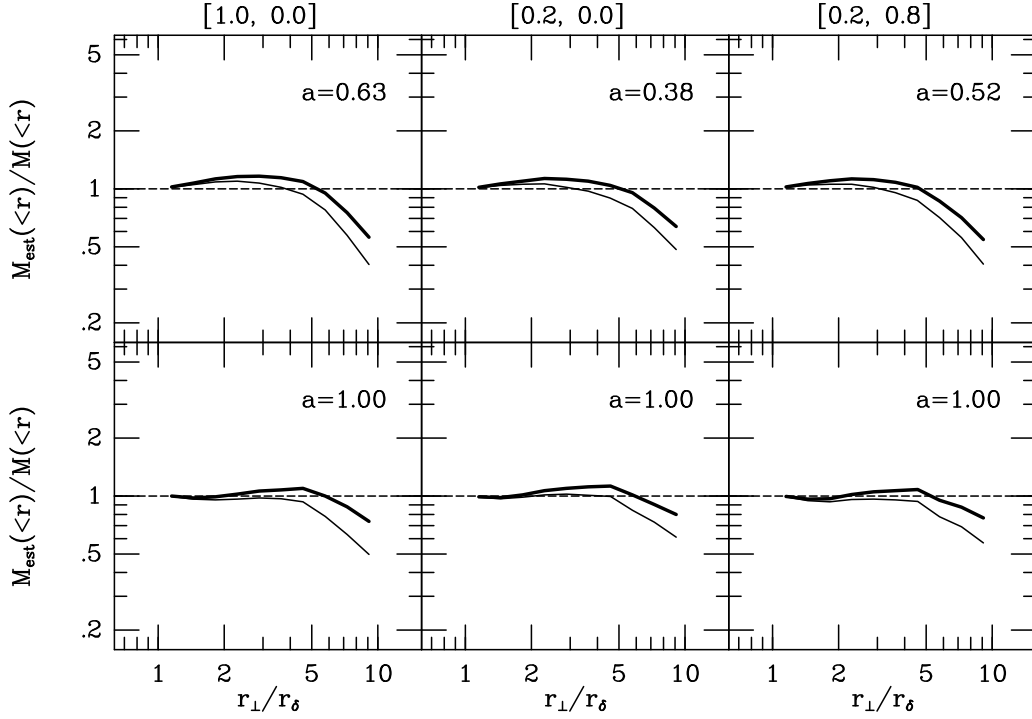
Fig. 4.— Ratio of the interior mass $M_{\rm est}(< r)$ estimated with equation (20) and the true interior mass $M(< r)$ of the most massive halo in each N-body model. We assume that we know r_δ and the virial mass $M(< r_\delta)$. Bold lines are for the filling function $\mathcal{F}_1 = 1/2$. Solid lines are for $\mathcal{F}_2 = [\ln(1 + 7r_\perp/r_\delta)]^{-1}$. Times are as in Fig. 3.
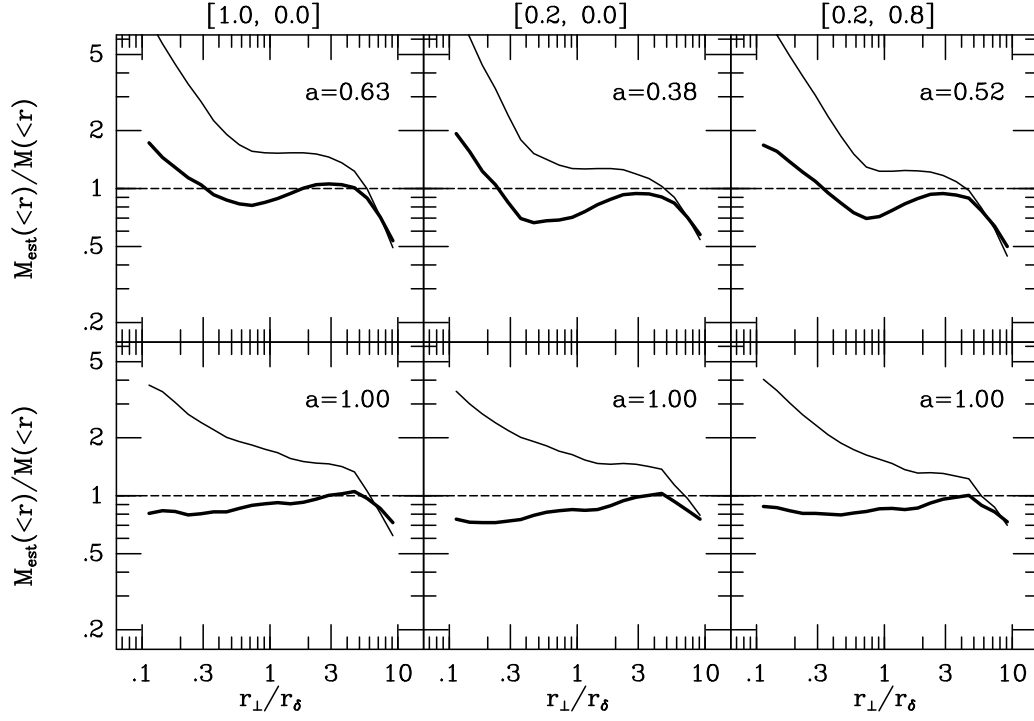
Fig. 5.— Same as Fig. 4, but we now assume that we do not know the virial mass $M(< r_\delta)$ and we integrate equation (20) from $r_\perp = 0$.
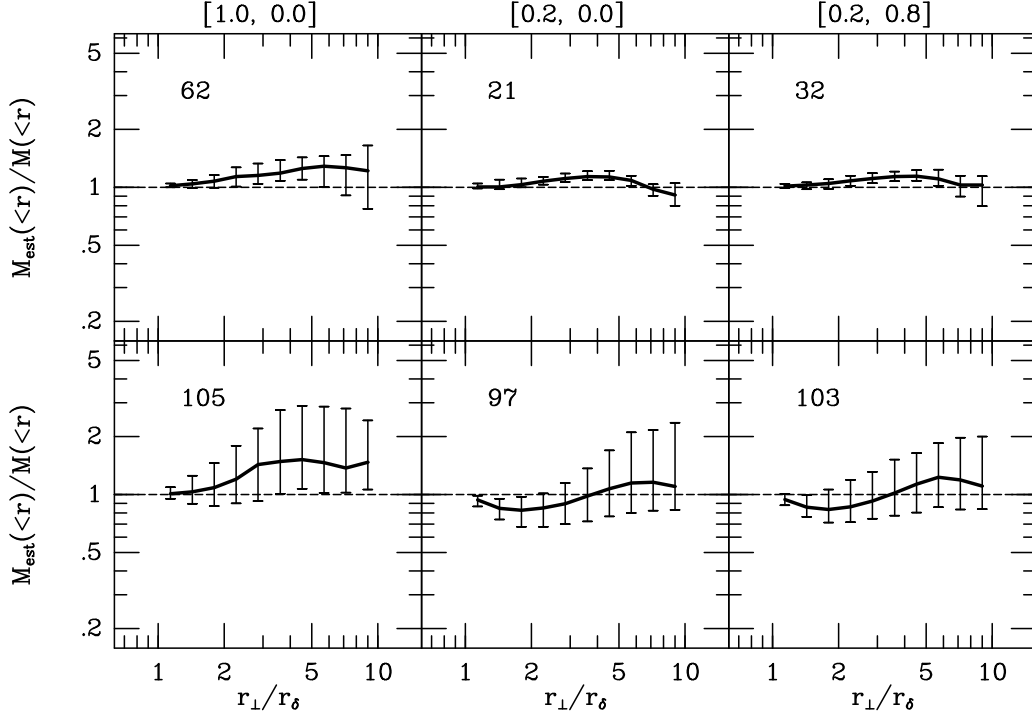
Fig. 6a.— Median mass profiles of halo samples in each N-body model. Masses are estimated with equation (20), assuming we know each $M(< r_\delta)$. Upper rows show the most massive halos: $M(< r_\delta) \geq 10^{14} M_\odot$ for the flat model, and $M(< r_\delta) \geq 2 \cdot 10^{13} M_\odot$ for the open models. Lower rows show the least massive halos: $10^{13} M_\odot \leq M(< r_\delta) < 10^{14} M_\odot$ for the flat model, and $10^{12} M_\odot < M(< r_\delta) \leq 2 \cdot 10^{13} M_\odot$ for the open models. Numbers of halos in each sample are shown. Error bars indicate upper and lower quartiles at each projected distance $r_\perp$. (a) Filling function $\mathcal{F}_1 = 1/2$; (b) filling function $\mathcal{F}_2 = [\ln(1 + 7 r_\perp / r_\delta)]^{-1}$.
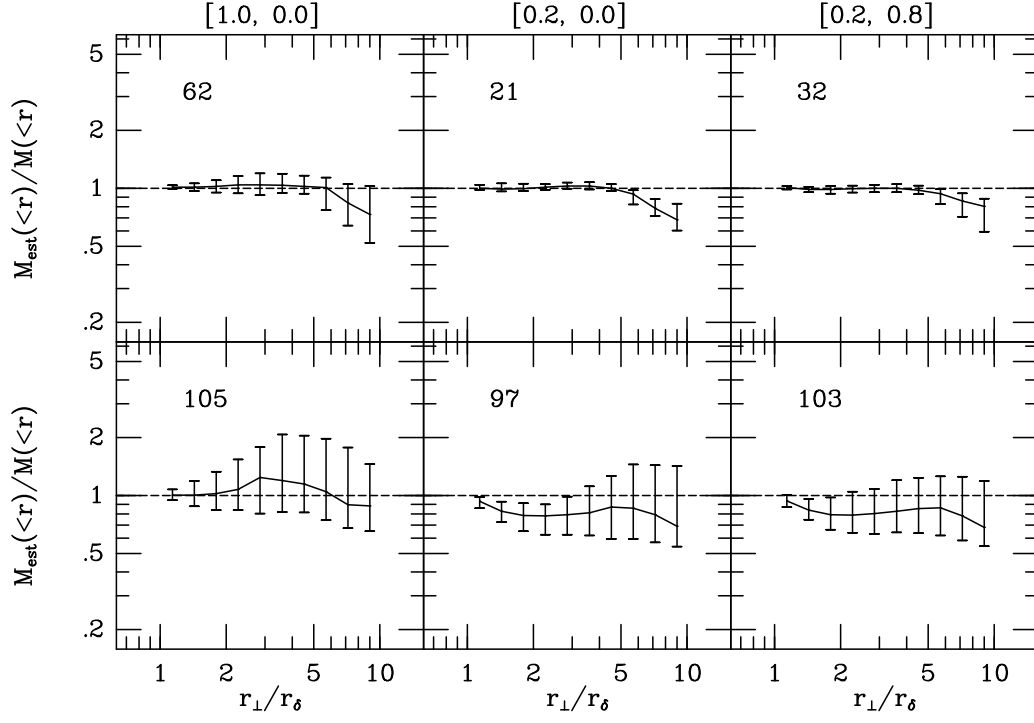
Fig. 6b.—